PLASTIC RELAXATION OF HIGHLY TENSILE STRAINED (100) Ge/InGaAs HETEROSTRUCTURES

Patrick Stephen Goley

Thesis submitted to the faculty of the Virginia Polytechnic Institute and State University
in partial fulfillment of the requirements for the degree of

Master of Science
In
Electrical and Computer Engineering

Mantu K. Hudait, Chair
Luke F. Lester
Jean J. Heremans

June 19th, 2015
Blacksburg, VA

Keywords: tensile, strain, germanium, misfit dislocations, stacking faults, plastic relaxation, elastic relaxation, Shockley partial dislocations

Copyright © 2015, Patrick Stephen Goley

PLASTIC RELAXATION OF HIGHLY TENSILE STRAINED (100) Ge/InGaAs HETEROSTRUCTURES

Patrick Stephen Goley

ABSTRACT

Biaxial tensile strain has been shown to greatly enhance the optoelectronic properties of epitaxial germanium (Ge) layers. As a result, tensile-Ge (ε_t-Ge) layers grown on larger lattice constant InGaAs or GeSn have attracted great research interest. However, no previous studies have investigated the plastic relaxation occurring in these ε_t-Ge layers. Here, we experimentally demonstrate that plastic relaxation occurs in nearly all ε_t-Ge epitaxial layers that are of practical interest for optoelectronic applications, even when layers may still exhibit strain-enhanced characteristics. We show arrays of misfit dislocations (MDs), which are mostly disassociated, form at the ε_t-Ge/InGaAs interface for ε_t-Ge layers as thin as 15 nm with less than 1% total mismatch. Wedge geometry of plain view transmission electron microscopy (PV-TEM) foils is utilized to carry out a depth dependent investigation MD spacing for a range of ε_t-Ge/InGaAs heterostructures. MD spacing measured by PV-TEM is correlated to ε_t-Ge layer relaxation measured by high-resolution x-ray diffraction. We confirm very low relaxation (< 10% relaxed) in ε_t-Ge layers does not imply they have been coherently grown. We demonstrate plastic relaxation in the ε_t-Ge layer is acutely sensitive to grown-in threading dislocations (TDs) in the template material, and that reducing TD density is critical for maximizing strain retention. Given that ε_t-Ge layer thicknesses of 150+ nm with greater than 1% tensile strain are desired for optoelectronic devices, this work suggests that MDs may inevitably be present at ε_t-Ge/InGaAs heterointerfaces in practical devices, and that the effect of MDs on optoelectronic performance must be better understood.

ACKNOWLEDGEMENTS

Foremost, I would like to thank my research advisor Professor Mantu Hutait for the *privilege* to conduct research under his advisement in the Advanced Devices and Sustainable Energy Laboratory (ADSEL) at Virginia Tech. The technical skills and knowledge I have gained while studying under his supervision will serve me well for the rest of my career.

I would also like to thank Professors Jean Heremans and Luke Lester for serving on my Thesis committee and providing constructive feedback and positive encouragement throughout my program of study.

I am extremely grateful for the personal mentorship and technical training provided to me by Dr. Christopher Winkler, as well as for his critical reading of this manuscript.

My sincere thanks also goes to the rest of the ADSEL team, Nikhil Jain, Yan Zhu, Michael Clavel, Peter Nguyen, and Jheng-Sin Liu, for their friendship and teamwork. Special thanks to Michael Clavel for performing the x-ray diffraction scans included in this work.

Thank you to my dear friend Christina McIntyre, the Interim Director of University Honors at Virginia Tech, without whom my path through this institution would have undoubtedly looked very different.

I would also like to express my deepest gratitude for the love and care of my wife Achmaa, the sustaining force in my life.

This material is based upon work supported by the National Science Foundation Graduate Research Fellowship under Grant No. DGE 0822220.

TABLE OF CONTENTS

ACKNOWLEDGEMENTS iii
TABLE OF CONTENTS iv
LIST OF FIGURES v
LIST OF TABLES vi

CHAPTER 1 1
INTRODUCTION 1
CHAPTER 2 5
MATERIAL AND METHODS 5
CHAPTER 3 8
RESULTS AND DISCUSSION 8
3.1 Bend Contours in PV-TEM 8
3.2 Misfit Dislocation Disassociation and Intersection Reactions 11
3.3 Depth Dependent Analysis of Misfit Dislocation Spacing and Energy Dispersive Spectroscopy 13
3.4 Sensitivity of Misfit Dislocation Spacing to Threading Dislocation Density. 17
3.5 Application of the Invisibility Criterion to Disassociated Misfit Dislocation 18
3.6 Strain Determination by High Resolution X-Ray Diffraction 20
3.7 Synthesis and Discussion of PV-TEM and HR-XRD Results 24
CHAPTER 4 27
CONCLUSION 27
REFERENCES 28
APPENDIX A 33
SUPPORTING FIGURES 33

LIST OF FIGURES

Figure 1. The three different layer structures utilized to obtain εt-Ge in this study: samples (a) S1, (b) S2, and (c) S3. The final indium composition and the amount of tensile strain in the Ge layer were each determined independently using HR-XRD reciprocal space mapping (i.e. coherent Ge growth was not assumed), and are therefore not linearly related here. 6

Figure 2. PV-TEM micrographs revealing the changing densities of MDs at εt-Ge/InGaAs interfaces in samples S1 (a)-(b), S2 (c)-(e) and S3 (f). The TEM foil thickness gradient allows simultaneous imaging of two distinct networks of MDs, one at εt-Ge/InGaAs interface and another in the graded InxGa1-xAs buffer as shown in (c) and (d).............. 10

Figure 3. A magnification stacking fault ribbons shown in Figure 2(d). The presence of stacking faults is direct evidence MDs disassociated in to SPDs. 13

Figure 4. A diagram of the wedge shape of the TEM foil loosely mapped to three overlapping PV-TEM micrographs of the same foil. The wedge geometry of the foil allows for the depth dependent investigation of the MD density. 15

Figure 5. (a) A PV-STEM micrograph of a region close to the edge of the S2 foil. An EDS elemental map of exactly the same region was integrated across the full height of the image to create an elemental line profile which is overlaid in (b) (the line profile direction is indicated by the horizontal aqua line in the image center). The image reveals that one network of MDs is located at the ε_t-Ge/InGaAs interface. 16

Figure 6. Quantitative contrast analysis of two orthogonal MDs. The dotted blue lines represent histogram line profiles of the intensity from the dislocation intersection shown in the top right of Figure 2(a). The dislocation parallel to g has measurably reduced contrast. 20

Figure 7. HR-XRD reciprocal space mappings of the (115) reflections for the three material stacks in this work. The maps are aligned by their GaAs peaks, allowing for a qualitative comparison of the tensile strain in the ε_t-Ge layer in each sample. 23

Figure A1. A cross-sectional TEM micrograph of the S2 materials stack showing the depth range of the InGaAs metamorphic buffer which contains a high density of misfit dislocations. The image also shows a smooth 2D surface morphology. 33

Figure A2. A cross-sectional TEM micrograph of the S3 materials stack. After S3 was grown, a small portion of the S3 wafer was cleaved and returned to the III-V growth chamber. A thin cap of InGaAs was grown to improve carrier confinement for optical characterization. The XTEM foil was prepared from this sample. As shown in the inset image, the InGaAs growth was 3D and the Ge growth was 2D. 34

Figure A3. PV-TEM micrograph of a portion of the S2 material stack in which the top 50-100 nm was chemically etched. No bend contours are observed. 34

Figure A4. An AFM micrograph showing the surface morphology of the S1 material stack. The image shows a 1D cross-hatch pattern and an array of shallow depressions. 35

Figure A5. An AFM micrograph showing the surface morphology of the S2 material stack. The image shows a 2D cross-hatch pattern and an array of shallow depressions less pronounced than those shown in Figure A4. 35

LIST OF TABLES

Table 1. The strain states of the InGaAs constant composition and ε_t-Ge layers, and the MD spacings for all three ε_t-Ge/InGaAs structures in this work. 24

CHAPTER 1

Introduction

The incorporation of biaxial tensile strain has been shown to greatly enhance the optical properties of Germanium (Ge) epitaxial layers.[1-2] Ge is uniquely suited to strongly benefit from tensile strain since it's direct bandgap is only ~0.14 eV larger than its indirect bandgap – a property that distinguishes it from silicon (Si) and other indirect bandgap semiconductors.[3] As a result of this property, relatively small amounts of tensile strain in Ge can have a proportionally large impact on carrier distributions within the conduction band, especially in the presence of elevated dopant levels.[4] Significant boosts to optical emission efficiencies have been demonstrated,[5-6] and due to a strain-induced reduction of the direct bandgap, the wavelength absorption range of Ge-based photodetectors can be usefully extended for optical communications applications.[7-8] Furthermore, tensile-Ge (ε_t-Ge) based devices can be heterogeneously integrated onto Si wafers.[9-10] This integration potential is what unlocks the most compelling application for ε_t-Ge based optoelectronic devices - on-chip optical interconnects. As data rates increase, it is becoming increasingly more challenging to transmit signals electrically with conventional copper interconnects.[11-12] An enticing approach to the interconnects bottleneck would be monolithic integration photonic devices with Si microprocessors. Si-based optoelectronics would be an obvious choice, however, the indirect bandgap of Si limits the realization of Si-based photonic devices. A versatile optoelectronic material compatible with Si has been an ambition of the

optoelectronics research community for decades and ε_t-Ge is emerging as a contender that may soon fulfill this long held dream.

Several methods have been proposed to achieve a ε_t-Ge layer.[1, 6, 13-15] One method takes advantage of the thermal expansion coefficient mismatch between Ge and Si by growing a thick (> 200 nm) layer of Ge that is relaxed at high temperature (> 600°C) .[15] After the wafer is cooled the Ge is tensile strained due to the thermal mismatch. The advantage of this method is that plastic relaxation of strain during growth with increasing Ge layer thickness is not a concern since the Ge layer is grown deliberately relaxed. The disadvantages are that the maximum tensile strain that can be achieved is ~0.3% and that high growth temperatures are required (600°C to 900°C). Other methods incorporate the strain mechanically. Up to 2% biaxial tensile strain was obtained by applying high-pressure gas to a 24 nm thick Ge nanomembrane.[1] Another mechanically straining method utilized a tungsten stressor layer applied to a Ge membrane formed by back-etching a region of Si from a Ge/Si bonded wafer.[6] 1.1% strain was obtained locally over the stressor using this method. Beyond mechanically straining methods and the thermal mismatch method, there is the method of growing ε_t-Ge epitaxially on a larger lattice constant material, usually InGaAs[2, 13, 16-17] or GeSn.[8, 14, 18] This method will hereafter be referred to as the strained epitaxy method and is the focus of this work.

The strained epitaxy method is attractive, and perhaps the most promising, since (i) it allows precise tailoring of the amount of strain by modulating the indium (In) or tin (Sn) composition in the buffer layer, (ii) it can incorporate a wide range of strain (up to and exceeding 1% is routinely achieved), and (iii) the area of the strained region is only limited by the size of the wafer. However, when the ε_t-Ge layer thickness is larger than the critical layer thickness for a given misfit, the film will begin to relax plastically by the introduction of misfit dislocations (MDs)

directed along orthogonal in-plane <110> directions, resulting in some loss of the performance enhancing tensile-strain. Theoretical prediction of the critical layer thickness has been treated by a number of papers.[19-22] Most of these predictive models agree that formation of MDs becomes favorable beyond a few tens of nm for ε_t-Ge with ~1% strain. This is the greatest limitation of the strained epitaxy method, since ε_t-Ge layer thicknesses of at least 150-200 nm are needed to achieve a laser.[23] Despite this limitation, many promising results have been reported so far. Bai *et al.* showed that lower ε_t-Ge growth temperatures on InGaAs by metal-organic chemical vapor deposition (MOCVD) helped to suppress strain relaxation by formation of MDs.[13] They achieved 0.58% ε_t-Ge in a thin (~25 nm) film and 1.37% ε_t-Ge in a similarly thin layer where island growth morphology was observed. High levels of strain can lead to non-planar epitaxial growth, or surface roughening by formation of islands or pits on the growth surface, since the energy barrier for elastic relaxation by surface roughening is lower than the energy barrier for plastic relaxation by dislocation introduction for layers above a critical strain level.[24] Wirths *et al.* obtained a planer 50 nm thick layer with 1.2% tensile strain by growing on $Ge_{0.904}Sn_{0.096}$.[18] Kersauson *et al.* achieved 0.75% ε_t-Ge at a thickness of 150 nm growing on a template of $In_{0.13}Ga_{0.87}As$. Higher strain levels, as high as 2.33%, have also been reported for very thin layers (~10 nm).[2] Most of these prior works demonstrate growth of ε_t-Ge beyond the predicted critical layer thickness where dislocations are expected to be introduced at the ε_t-Ge/InGaAs heterointerface. *However, no prior works have reported direct observation of these dislocations by plan view transmission electron microscopy (PV-TEM), or investigated how the density of these dislocation arrays changes on various growth templates and evaluated their respective contributions to any loss of tensile strain.* Such knowledge is essential to understand the amount of strain that can be incorporated in Ge by strained epitaxy. Here, we demonstrate experimentally that arrays of MDs exist at ε_t-Ge/InGaAs

heterointerfaces, as shown by direct observation in PV-TEM micrographs, even for layers as thin as 15 nm with less than 1% tensile strain. We analyze the densities of these MD arrays as they are formed on different InGaAs templates and calculate their respective contributions to the total relaxation which is determined by high resolution x-ray diffraction. The range of In compositions (14-22%) and Ge layer thickness (15-30 nm) utilized for this study are particularly important since they are at or near the boundary where pseudomorphic Ge growth is expected to be possible based on predictions of critical layer thickness in the literature.[19, 21, 25] Utilizing TEM we investigate the depth dependence of the MD spacing, and confirm MD disassociation into Shockley partial dislocations (SPDs) by imaging of stacking fault ribbons and separately by diffraction vector (**g**-vector) analysis. These new results provide great insight into the ultimate limits of the strained epitaxy method.

CHAPTER 2

Material and Methods

Three different layer structures were grown by solid-source molecular beam epitaxy (MBE) for this study. Our facility is equipped with two separate MBE chambers which are dedicated for III-V and Ge growth, respectively, and are connected by an ultra-high vacuum transfer chamber. The layer structures, summarized in Figures 1a, 1b, and 1c, will hereafter be referred to as S1, S2, and S3 respectively. In samples S1 and S2, we have started from a semi-insulating (100) GaAs substrate with a 2° offcut. Substrate oxide desorption took place at ~750^oC under an arsenic over pressure of ~10^{-5} Torr and was monitored by *in-situ* reflection high-energy electron diffraction. Next, a GaAs buffer was grown to improve the starting surface for an $In_xGa_{1-x}As$ linearly-graded metamorphic buffer. The $In_xGa_{1-x}As$ compositional grading rates were 35.6% and 22.2% In per micron for S1 and S2, respectively. The graded buffers were each capped with 500 nm of constant composition $In_xGa_{1-x}As$ with $x = 0.18$ and 0.22 for S1 and S2, respectively. The In compositions x are determined directly from the relaxed lattice constant as measured by high resolution x-ray diffraction (HR-XRD). The wafers were then cooled and transferred under ultra-high vacuum (~10^{-10} torr) to the Ge growth chamber where 15 nm and 30 nm of Ge was grown on samples S1 and S2, respectively, at 400^oC (thermocouple temperature). The starting surface for S3 was a Si (100) substrate with a 6° offcut towards the <110> direction. After oxide desorption, a 2.7 μm GaAs buffer was grown to create a GaAs "virtual substrate" on Si. This buffer growth procedure has been described elsewhere.[26] The growth following the GaAs buffer

proceeded the same as for S1 and S2 but with an indium compositional grading rate of 11.9% per micron and a final In composition of 14%. We included this third sample grown on a GaAs-on-Si substrate, which is expected to have a much higher threading dislocation density (TDD) due to the large lattice mismatch between GaAs and Si (3.93%), to investigate the impact of threading dislocations on ε_t-Ge relaxation.

(a)	(b)	(c)
0.7% ε_t-Ge (15 nm)	1.2% ε_t-Ge (30 nm)	0.6% ε_t-Ge (30 nm)
$In_{0.18}Ga_{0.82}As$ (500 nm)	$In_{0.22}Ga_{0.78}As$ (500 nm)	$In_{0.14}Ga_{0.86}As$ (700 nm)
$In_xGa_{1-x}As$ (500 nm) Linear graded buffer x: 0.03 → 0.18	$In_xGa_{1-x}As$ (1000 nm) Linear graded buffer x: 0.03 → 0.22	$In_xGa_{1-x}As$ (1200 nm) Linear graded buffer x: 0.03 → 0.14
GaAs buffer (220 nm)	GaAs buffer (250 nm)	GaAs buffer (2700 nm)
GaAs (100) 2°	GaAs (100) 2°	Si (100) 6°

Figure 1. The three different layer structures utilized to obtain εt-Ge in this study: samples (a) S1, (b) S2, and (c) S3. The final indium composition and the amount of tensile strain in the Ge layer were each determined independently using HR-XRD reciprocal space mapping (i.e. coherent Ge growth was not assumed), and are therefore not linearly related here.

Plan-view electron transparent foils of each sample were prepared for examination in a JEOL 2100, 200 keV transmission electron microscope equipped with energy-dispersive x-ray spectroscopy (EDS) and a beryllium double-tilt holder. The foils were prepared by mechanical polishing, dimpling, and finally low-temperature (-120 °C) Ar^+ ion milling from the substrate side only. The liquid nitrogen cooling during milling prevents any heating that the foil would otherwise experience due to ion bombardment, thus preserving as-grown dislocations networks. Cooling also improves the chamber vacuum by cold trapping, therefore reducing redeposition of sputtered material on the foil surface. Cross-sectional foils of S2 and S3 were prepared in a similar fashion

for layer thickness, growth rate, and grading rate determination. Cross-sectional TEM micrographs of these foils are provided in Figures S1 and S2 in the supporting information (see Appendix A) for samples S2 and S3, respectively. Each layer structure was characterized by HR-XRD reciprocal space mapping of the (004) and (115) reflections with a PANalytical X-Pert Pro system. These reciprocal lattice points were utilized to confirm the relaxed lattice constant and corresponding In composition in the constant composition InGaAs layer. Independently, the (115) reflections of the Ge peaks where utilized to determine the in-plane lattice constant of the ε_t-Ge layer, allowing precise determination of strain amount. The surface morphology of the S1 and S2 structures were investigated by a Bruker Dimension Icon atomic force microscope (AFM) operating in ScanAsyst mode. AFM was performed to look for the cross-hatch pattern which is the surface morphological signature of a well relaxed graded buffer layer. AFM was also utilized to look signs of islanding or pit formation which can become energetically favorable in strained layer growth due to their ability to relieve strain elastically.[24]

CHAPTER 3

Results and Discussion

3.1 Bend Contours in PV-TEM

A series of PV-TEM micrographs of the three samples in this study (S1, S2, S3) are shown in Figure 2. One feature common throughout all the samples is an abnormally high density of bend contours (BCs). The dark bands, or BCs, are due to the lattice moving into and out of different Bragg diffracting conditions and their presence indicates slight bending in the specimen foil. We speculated the high density of BCs was due to the ability of the sample foil to relieve tensile strain in the ε_t-Ge elastically by foil bending once a critical thickness of the underlying relaxed InGaAs template had been polished and ion milled away. To test this hypothesis a second foil was prepared, using the exact same method, from a small portion of S2 in which the top 50-100 nm was chemically etched – completely removing the ε_t-Ge layer. No strong BCs were observed in this foil, shown in a PV-TEM micrograph included in Figure S3 in the supporting information. This result suggests the existence of BCs in high densities is direct physical evidence of high tensile strain in the Ge layer. The BCs complicate the TEM analysis of these foils by obscuring clear views of dislocations under a uniform diffraction condition. Our observations indicate that a critical InGaAs thickness of approximately 900 nm is needed to sufficiently minimize foil bending and obtain large flat regions (at least ~5 μm^2) without BCs. This presents a natural tradeoff since these thicker regions are challenging to image due to more of the incident electron beam being absorbed in the foil resulting in reduced image clarity. We had the most success in obtaining clear images of these extremely thick regions (~ 1 μm) by tilting the foil to strong low-index two-beam

conditions and inserting the objective aperture to reduce inelastic scattering. This strategy allowed us to use longer than usual exposure times (5-10 seconds) in order to capture clear and detailed TEM micrographs, shown in Figure 2.

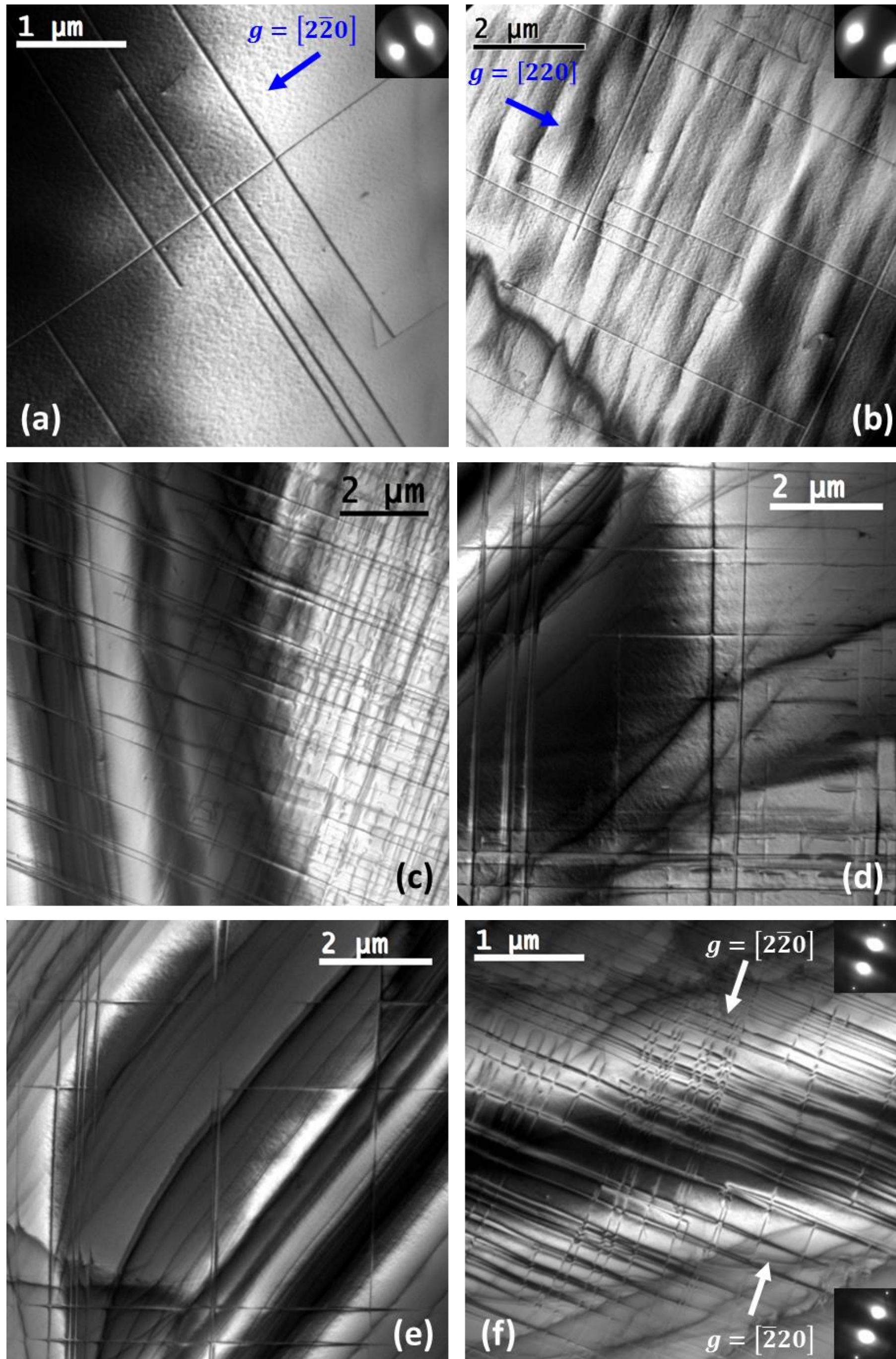

Figure 2. PV-TEM micrographs revealing the changing densities of MDs at εt-Ge/InGaAs interfaces in samples S1 (a)-(b), S2 (c)-(e) and S3 (f). The TEM foil thickness gradient allows simultaneous imaging of two distinct networks of MDs, one at εt-Ge/InGaAs interface and another in the graded InxGa1-xAs buffer as shown in (c) and (d).

3.2 Misfit Dislocation Disassociation and Intersection Reactions

Despite the BCs, MDs running in orthogonal in-plane <110> directions are clearly observed in all three samples. We do, however, note differences in the densities and in the character of the dislocation networks in the different samples. Images of S1, shown in Figure 2(a) and 2(b) show MD segments shorter in length and with larger spacing compared to S2 and S3. Dislocation spacing measurements for all three samples are provided in Table 1. The local strain fields of MDs are expected to occasionally react when orthogonal MDs intersect. These strain field reactions can cause MDs to repel each other resulting in L-reactions (both MDs change their glide direction by 90°).[27] Interestingly, no L-reactions are counted at dislocation intersections in the thinner regions of the S1 foil. L-reactions are statistically expected to occur at 16-25% of MD intersections in diamond and zincblende materials when all dislocations have the usual **b** = ½ <110> type Burgers vectors.[27] Sample S2 showed an array of dislocations similar to S1 but with much longer dislocation segments that were more closely spaced, as seen in Figures 2(c), 2(d), and 2(e). The difference in dislocation spacings between S1 and S2 is best seen by comparing Figure 2(b) and 2(e). As in S1, we counted no L-reactions at intersections in the thin regions of the S2 foil. We explain the absence of L-reactions in the following way. MDs in diamond or zincblende materials glide in {111} slip planes and have Burgers vectors of the type **b** = ½ <110> usually angled 60° from the dislocation line. Normally, such dislocations can easily cross-slip from one {111} plane to another. However, these MDs can also disassociate into Shockley partial dislocation (SPD) pairs with Burgers vectors of the type **b** = 1/6 <112>. Furthermore, although it has not yet been shown in the Ge/InGaAs material system, MD disassociation has been shown to occur in tensile (100) oriented films in other material systems.[25, 28-31] This is due to the fact that the tensile (100) growth direction configuration is one in which the leading SPD of a SPD pair, the 90° partial, is pure edge

component and has its Burgers vector completely aligned with the resolved shear stress on the {111} planes, i.e. the misfit stress acts on the 90° partial very efficiently. Other configurations where this occurs are compressive (110) and (111) growth.[28] Due to the alignment of the leading SPD Burgers vector and the resolved shear stress, MDs nucleate easier in these configurations, resulting in a downward shift in the critical layer thickness compared to compressive (100) growth.[31-32] If the MDs near the surface were disassociated it would help explain their straightness since a SPD cannot cross-slip. Its Burgers vector lies in a single {111} plane and its glide motion is restricted to this unique plane.[33] As a result, intersecting orthogonal SPDs should interact less frequently since they have fewer degrees of freedom to respond to local strain fields. This reduced interaction behavior by disassociated MDs at a tensile mismatched (100) interface was also noted by Maree *et al.* for Si/GaP(100).[25] A similar network of remarkably straight MDs was also reported by Hirashita *et al.* for thin layers (10 - 25 nm) of tensile strained Si grown on $Si_{1-x}Ge_x$ with x = 0.10 – 0.15.[30] This group also concluded the MD network was comprised of 90° SPDs. Upon careful examination of micrographs of samples S2 and S3 the characteristic fringes of stacking faults, which are created when disassociation occurs, were observed running in parallel with many MDs. Therefore, absence of L-reactions in the dislocation networks in the thin regions of S1 and S2 is attributed to these networks being primarily disassociated 60° dislocations. Stacking fault ribbons are clearly seen in Figure 3, a magnification of the top left corner of Figure 2(d), although in most cases the bands of fringes are very narrow (< 50 nm) with only 2 or 3 visible fringes. This is due to a stacking fault length which is limited by the 30 nm height of the ε_t-Ge film, which also explains why fringes are less clear in the S1 foil where the ε_t-Ge layer thickness is only 15 nm.

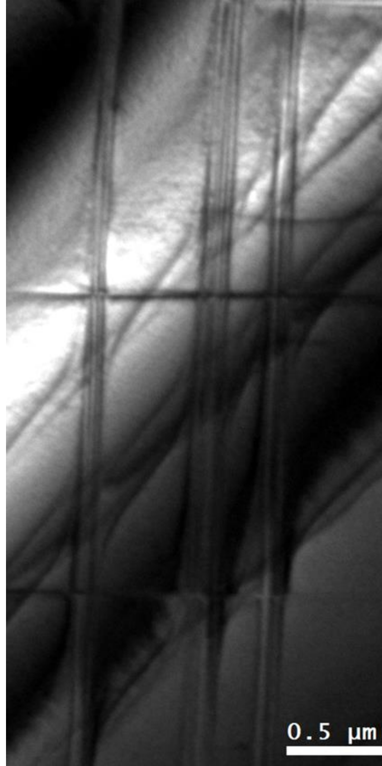

Figure 3. A magnification stacking fault ribbons shown in Figure 2(d). The presence of stacking faults is direct evidence MDs disassociated in to SPDs.

3.3 Depth Dependent Analysis of Misfit Dislocation Spacing and Energy Dispersive Spectroscopy

Figure 2(c) shows two vertical running BCs in the left half of the image. In the right half of the image no BCs are present since the InGaAs is thick enough to sufficiently suppress foil bending. However, this region also shows a very high density of MDs. Figure 4 represents visual explanation for why two distinct dislocations networks are seen in Figure 2(c). The foils have a wedge geometry as depicted in the diagram, which is loosely mapped to three micrographs of S2 fitted together, also shown in Figure 4. As one moves up the foil thickness gradient, deeper regions of the growth enter into the foil and hence, into view in the micrographs. The visibility of the

denser second network of MDs is an indication that the InGaAs graded buffer layer has entered into the foil thickness. The foil bending at the tip due to the strain is small on the scale of the diagram in Figure 4 and is not included. The angle of the foil wedge was estimated using the measured horizontal distance d_1 from the wedge tip to the point where the very high density MDs come into view, and the depth d_2 of the InGaAs graded buffer MD network as measured by cross-sectional TEM. The angle was estimated as $\tan^{-1}(d_2/d_1) \approx 3.5^{o}$. The increase in frequency and decrease in width of the BCs closer to the wedge tip, as seen in Figure 4, is a characteristic of higher-order bend contours and indicate stronger bending closer to the tip.[34] This supports our earlier conclusion that the ε_t-Ge layer is able to relieve an increasing amount of strain elastically in the thin TEM foil by bending as there is less and less InGaAs thickness to support it. These higher-order BCs completely obscure the image contrast of the dislocations. A scanning TEM (STEM) micrograph of S2, shown in Figure 5(a), shows that these dislocation run almost to the very tip of the wedge, and only drop out of view when the constant composition InGaAs layer is no longer in the foil thickness. To confirm that the point at which the dislocations disappear is point the foil becomes pure Ge, characteristic x-rays were collected from each point in the image shown in Figure 5(a) to produce an EDS elemental map. The elemental data in the map was integrated across the full height of the image to generate an elemental line profile, shown in Figure 5(b), directed along the horizontal aqua line in the center of the figure. The termination of the MDs does indeed coincide with the termination of the indium, gallium, and arsenic characteristic x-rays. We also observe that the MD density is essentially constant between the point where the InGaAs first enters into the foil thickness near the tip and the point where the density spikes as the InGaAs graded buffer enters into the foil thickness. These data confirm that (i) the InGaAs constant

composition layer is mostly free of MDs, and (ii) the straight line, lower-density MD array near the surface is located at the ε_t-Ge/InGaAs heterointerface.

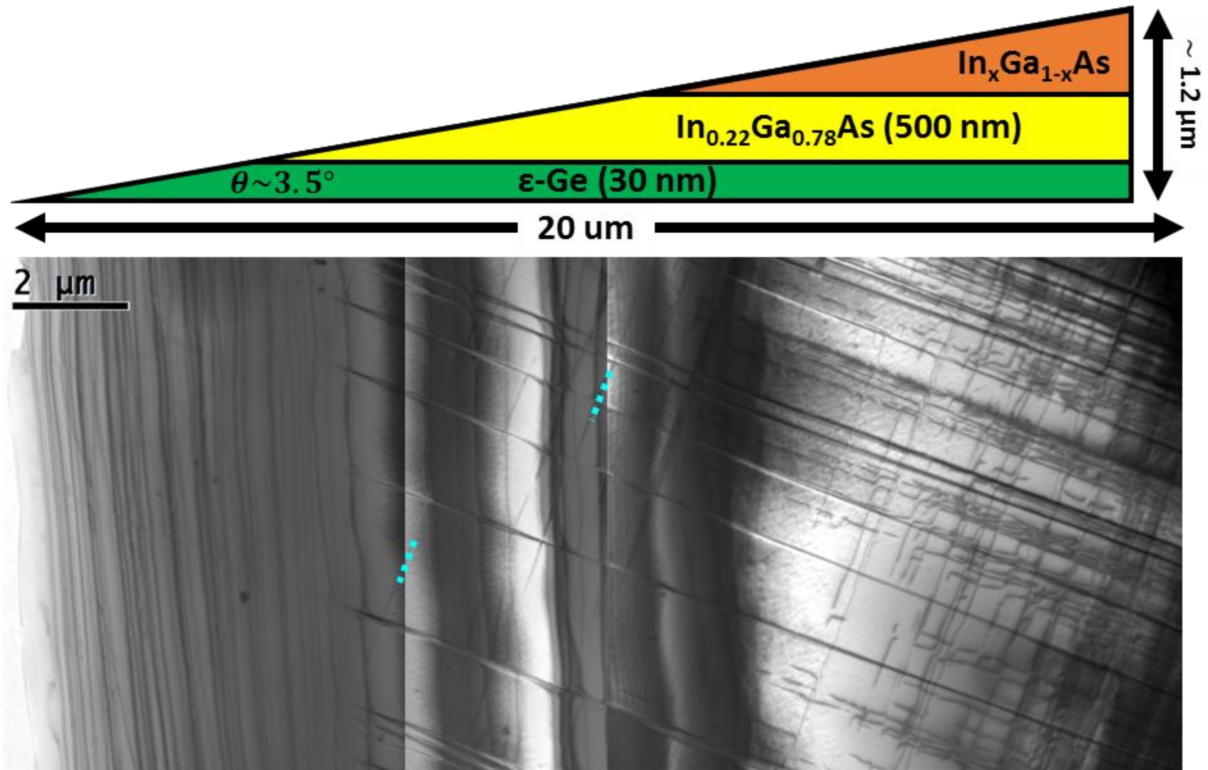

Figure 4. A diagram of the wedge shape of the TEM foil loosely mapped to three overlapping PV-TEM micrographs of the same foil. The wedge geometry of the foil allows for the depth dependent investigation of the MD density.

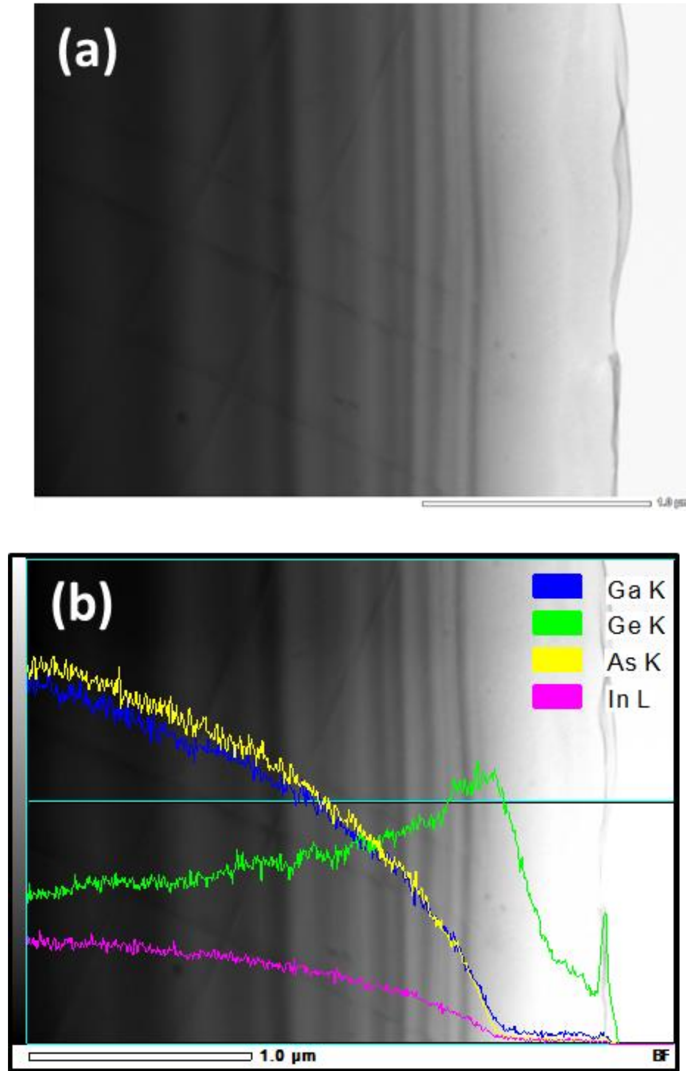

Figure 5. (a) A PV-STEM micrograph of a region close to the edge of the S2 foil. An EDS elemental map of exactly the same region was integrated across the full height of the image to create an elemental line profile which is overlaid in (b) (the line profile direction is indicated by the horizontal aqua line in the image center). The image reveals that one network of MDs is located at the ε_t-Ge/InGaAs interface.

The ε_t-Ge/InGaAs MD array in the S3 foil shows much a higher density in each orthogonal direction which is notable since it also has the lowest indium composition. These higher densities

are observed in thin regions with BCs, as shown in Figure 2(f), and so they cannot be attributed to the linear graded buffer. Two selected area diffraction patterns taken from just above and just below the dark band in Figure 2(f), shown in the insets, reveal the classic BC characteristic of inverse diffraction vectors, or **g** vectors, on each side of the contour. The array is again characterized by long straight dislocations, although intersections appear less sharp generally due to stronger overlapping of the strain fields of the more closely spaced dislocation lines. These strain fields make identifying L-reactions and dislocation dipoles difficult, particularly in the presence of BCs and stacking fault fringes. However, observation of stacking fault ribbons in sample S3 indicates many MDs here also disassociated, as they are in S1 and S2.

3.4 Sensitivity of Misfit Dislocation Spacing to Threading Dislocation Density

The dissimilarity in dislocation spacing between the S1/S2 foils and the S3 foil indicates plastic relaxation in ε_t-Ge films is acutely sensitive to the grown-in TDD in the growth template. TDD has been measured by PV-TEM for the S1 and S2 structures and is listed in Table 1. Due to the much higher TDD in S3 it has been estimated by cross-sectional TEM since the high density of MDs obscures the view of threading dislocations at the surface. Given that the S3 structure leads to a much denser MD network, despite it having a reduced ability to build elastic strain energy (due to the lower mismatch), it indicates that the SPDs form by different mechanisms with different energy barriers when grown-in threading dislocations are available. In the S3 structure the grown-in threading dislocations propagating up from the GaAs buffer are bent into the ε_t-Ge/InGaAs interface by the elastic misfit stress to form an orthogonal array of perfect MDs with burgers vectors **b** = ½ <110> as described by Matthews and Blakeslee.[21] However, due to high availability of existing threading dislocations, the need for nucleation of half-loops at the surface is diminished. Then the perfect MDs disassociate such that the leading 90° partial glides up towards the surface

in a (111) plane creating a stacking fault in the process, while the trailing 30° partial remains pinned at the ε_t-Ge/InGaAs interface. As strained layer thickness increases, the trailing partial should eventually leave the interface due to the dislocation-dislocation attractive force caused by stacking fault energy. However based on the range of stacking fault band widths observed in the S3 foil the equilibrium separation between the leading and trailing partials appears to be sensitive to the local strain conditions. In the S1 and S2 structures the mechanism described above is constrained by the need to nucleate half-loops at the surface due to a scarcity of grown-in threading dislocations, resulting in reduced plastic relaxation in the ε_t-Ge layer, as shown in qualitatively in Figure 2 and quantitatively in Table 1.

3.5 Application of the Invisibility Criterion to Disassociated Misfit Dislocation

A complete Burgers vector analysis by the invisibility criterion $\boldsymbol{g} \cdot \boldsymbol{b} = \mathbf{0}$ was not successful. This is largely due to the inability to maintain a constant **g** vector over a sufficiently large region in a bent specimen foil. Moving to thicker regions where bending was minimized was not effective since these extremely thick regions give substantial dynamical diffraction contrast due to the diffracted beam being rediffracted multiple times, weakening the two-beam condition. However, in moderately thick regions (~ 400 nm) a constant low index <220> type **g** vector could be obtained over small areas, a few μm^2, as shown in Figure 2(a). Working within these limitations, we observed that MD lines parallel to the **g** vector at the ε_t-Ge/InGaAs interface retain significant residual contrast. This is shown in Figure 2(a), (b), and (f), and is also examined quantitatively in Figure 6, which is a magnification of the image given in Figure 2(a). Dislocations lines in the S1 foil parallel to a <220> type **g** vector gave ~40% less contrast than lines perpendicular to **g**, as measured in Figure 6. As previously discussed, the MDs are expected to be disassociated perfect 60° dislocations, with the separation distance between the partials being constrained by the 15 nm

height of the ε_t-Ge film. A 60° dislocation with its line directed along the $[\bar{1}10]$ direction, as shown in Figure 2(a), with Burgers vector **b** = ½ $[\bar{1}01]$ will disassociate into a leading 90° partial with **b** = 1/6$[\bar{1}\bar{1}2]$ and a trailing 30° partial with **b** = 1/6$[\bar{2}11]$. If **g** is set to $[2\bar{2}0]$ as in Figure 2(a), the leading pure-edge dislocation should vanish since both $\boldsymbol{g} \cdot \boldsymbol{b}$ and $\boldsymbol{g} \cdot (\boldsymbol{b} \times \boldsymbol{u})$ are both equal to zero, where $\boldsymbol{u}$ is a unit vector parallel to the dislocation line.[35] However, the trailing 30° partial will not lose contrast since $\boldsymbol{g} \cdot \boldsymbol{b} = -\mathbf{1}$. At the scale of the image in Figure 2(a), the contrast caused by the leading and trailing dislocations are virtually overlapping due to the narrow separation of the partials. Therefore, when the leading partial loses contrast due to the diffraction condition we should still see a dislocation line due to the trailing partial, but the total contrast should be measurably reduced. This behavior is exactly what we have observed. The loss of contrast appears to occur primarily on one side of the dislocation line, reflecting the non-zero separation distance between the leading (invisible) and trailing (visible) partials.

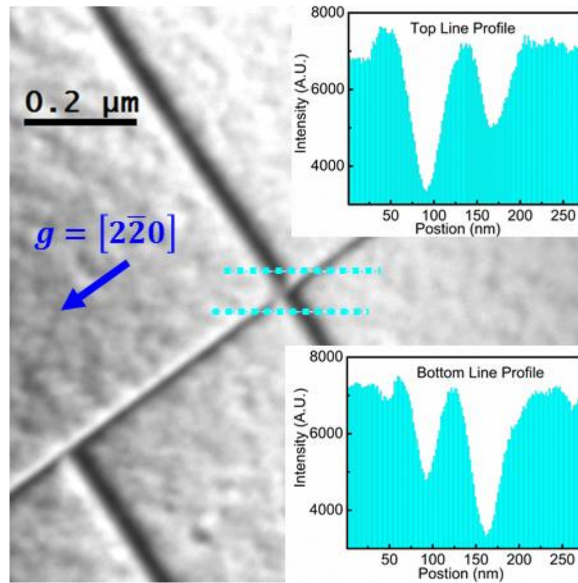

Figure 6. Quantitative contrast analysis of two orthogonal MDs. The dotted blue lines represent histogram line profiles of the intensity from the dislocation intersection shown in the top right of Figure 2(a). The dislocation parallel to g has measurably reduced contrast.

3.6 Strain Determination by High Resolution X-Ray Diffraction

Figure 7 shows the reciprocal space mappings (RSMs) of the (115) reflections for the S1, S2, and S3 wafers. The maps have been aligned vertically by their GaAs peaks, marked by the red dotted line, to facilitate a qualitative comparison of strain. The most highly strained sample S2 is placed at the top. The aqua and orange dotted lines approximate the locations of 1.2% and 0.7% biaxial tensile strain, respectively, in the ε_t-Ge layer. The separation between 0.7% and 0.6% strain on this scale is approximately the thickness of the dotted lines so the 0.6% line is omitted for clarity. It is important to note that in each mapping the ε_t-Ge peak appears slightly to the right of the InGaAs constant composition layer peak. This is direct evidence that some degree of relaxation has taken place. The exact position of the ε_t-Ge peak in the S1 RSM is difficult to precisely

determine due the thinness of the layer. However, the highest peaks in the center of the island of intensity all give a value for the elastic misfit strain ε within the range of 0.72% ±0.05%. The elastic misfit strain of a given epilayer is calculated as

$$\varepsilon = \frac{a_{//} - a_e}{a_e} \tag{1}$$

where $a_{//}$ is the in-plane lattice parameter of the epilayer as extracted from its (115) RSM peak, and a_e is the relaxed lattice parameter of the same epilayer. Table 1 lists the In composition x_{In}, the degree of relaxation R_{In}, and the elastic misfit strain ε_{In} (negative sign indicating compressive strain) of the $In_xGa_{1-x}As$ constant composition layer. It is worthwhile to mention how each term in Table 1 is calculated in this work since slight variations exist in the literature. The degree of relaxation of a given epilayer is found by

$$R = \frac{a_{//} - a_s}{a_e - a_s} \tag{2}$$

where a_s is the in-plane lattice parameter of the template material upon which the epilayer is grown, i.e. for computing R_{Ge}, a_s is the extracted in-plane lattice parameter of InGaAs constant composition layer. The GaAs buffer layer for sample S3 is found to be 96.3% relaxed. The total misfit f is given by

$$f = \frac{a_s - a_e}{a_e} = \varepsilon + \delta. \tag{3}$$

Equation (3) also shows the relationship between f, ε, and the plastic misfit strain δ. The plastic relaxation δ allowed by an array of MDs with linear spacing S in each orthogonal direction is given by [20]

$$S = \frac{b_{eff}}{\delta} \tag{4}$$

where b_{eff} is the component of the Burgers vector in the interface-plane in the direction of the spacing. Our observations indicate that δ as calculated from f - ε, where f and ε are obtained from HR-XRD, can diverge significantly from δ as calculated from b_{eff} / S, where S is obtained from PV-TEM, when $S >> 10S^*$, and S^* is the spacing required to fully relax the misfit. Therefore, in this work we have denoted δ as calculated from equation (3) as the total misfit relaxation δ_t, and δ as calculated from equation (4) as the plastic misfit relaxation δ_p. Since the relaxation is expected to be due to a mixture of 90° partial and perfect 60° dislocations, we have calculated δ_p for both cases. It is worth noting that the values for δ_p in Table 1 represent an upper bound since equation (4) assumes the length of the misfit segment is the full length of the growth surface, which is clearly not the case for S1, but is likely reasonable for S2 and S3.

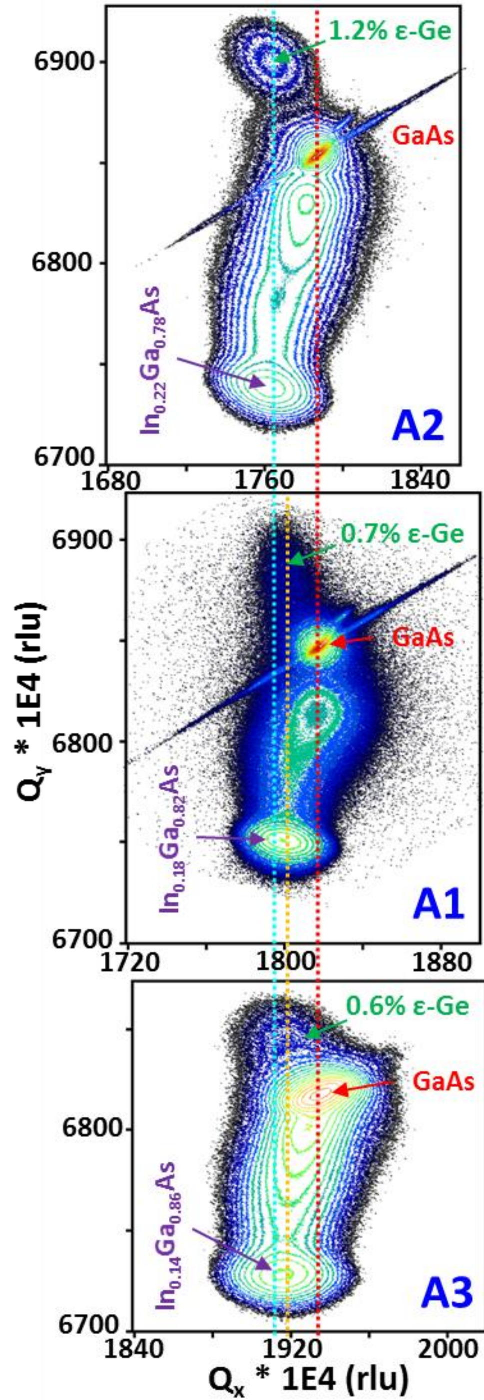

Figure 7. HR-XRD reciprocal space mappings of the (115) reflections for the three material stacks in this work. The maps are aligned by their GaAs peaks, allowing for a qualitative comparison of the tensile strain in the ε_t-Ge layer in each sample.

Table 1. The strain states of the InGaAs constant composition and ε_t-Ge layers, and the MD spacings for all three ε_t-Ge/InGaAs structures in this work.

	x_{In}	R_{In}	ε_{In}	f	R_{Ge}	ε_{Ge}	TDD (cm^{-2})	Observed spacings (nm)		δ_t	δ_p SPD	δ_p P60	S^*_{SPD} (nm)	S^*_{P60} (nm)
S1	17.8%	84.1%	-0.20%	0.99%	24.3%	0.74%	1.2E7	2200	4400	0.25%	0.004%	0.01%	14	20
S2	22.2%	89.3%	-0.17%	1.33%	7.8%	1.23%	<4E6	900	2000	0.10%	0.01%	0.02%	10	15
S3	14.3%	80.0%	-0.23%	0.70%	17.9%	0.58%	2E8	150	300	0.12%	0.59%	0.13%	19	29

3.7 Synthesis and Discussion of PV-TEM and HR-XRD Results

There are a number points to discuss related to the analysis presented in Table 1. First, by comparing f to ε_{Ge} we note that all three ε_t-Ge layers have retained most of the total misfit strain, despite the presence of MD arrays. This is true even in S3 which has a much higher linear density of dislocations in each orthogonal direction. For all three samples the PV-TEM and HR-XRD data reinforce each other since the observed dislocation spacings fall well short of the spacing S^* that would be required to fully relax the strain. Here, we have demonstrated experimentally that very low relaxation in ε_t-Ge layers ($R_{Ge} < 10\%$) does not imply coherent growth. Setting aside that MDs allow the performance enhancing tensile strain to erode away, they are also potentially electrically active defects and may facilitate increased non-radiative recombination,[36-37] which is highly undesirable in optoelectronic devices. Since we have shown that MDs exist even in a 15 nm thick ε_t-Ge layer with $f < 1\%$, a perfectly coherent 150+ nm thick layer with $\varepsilon_{Ge} > 1\%$ seems like a tremendous technological challenge. It may be advantageous to bypass the goal of perfectly coherent ε_t-Ge layer growth, and instead focus on methods to minimize relaxation and investigate MD tolerance in ε_t-Ge based optoelectronic devices.

The second point to discuss is the large discrepancy between δ_t and δ_p in S1 and S2. This is an indication that elastic relaxation, which occurs by surface deformation, is contributing to the total relaxation of the ε_t-Ge layer. Cross-sectional TEM of S2 showed a flat conformal 2D ε_t-Ge layer, suggesting any elastic surface deformation must be occurring over large areas. We investigated this possibility by AFM. AFM micrographs covering an area of 20 μm^2 show the surface morphology of S1 and S2, which have a root-mean-square (RMS) roughness of 2.51 nm and 3.35 nm, respectively. These micrographs are provided in Figures S4 and S5 in the supporting information for samples S1 and S2, respectively. The surface of S2 is dominated by a 2D cross-hatch pattern indicating good relaxation in the $In_xGa_{1-x}As$ linear graded metamorphic buffer. S1 has a weaker 1D cross-hatch pattern indicating less relaxation of the InGaAs, which is consistent with HR-XRD results. We attribute the difference in relaxation to the higher In grading rate utilized for S1. Although these cross-hatch patterns partially obscure the more subtle surface morphological features, small 1-2 μm^2 depressions 5-10 nm deep are seen on the surface. These depressions are more pronounced in S1, which supports the conclusion that these features may be related to the elastic relaxation observed in the S1 and S2 ε_t-Ge layers since the elastic relaxation is S1 is greater. Compared to S1 and S2, very little elastic relaxation is observed for S3. We believe this is an indication that the availability of grown-in threading dislocations lowers the energy barrier for plastic relaxation by introduction of MDs to a level below that of elastic relaxation by surface deformation. When threading dislocations are scarce however, plastic relaxation relies on the nucleation of half-loops which has a higher energy barrier, resulting in an active competition between plastic relaxation by introduction of MDs and elastic relaxation by surface deformation. The higher TDD of S1 compared to S2 is attributed to half-loops which are less expanded, i.e.

most of the treading dislocations counted in S1 are believed to be associated with half-loops rather than being grown-in.

Thirdly, the effect of residual strain energy in the growth template material on the ε_t-Ge layer has not been studied in previous works related to the strained epitaxy method. Although the reason for the increased elastic relaxation in S1 compared to S2 is not fully understood, we speculate it may be due to the higher level of residual compressive strain in the InGaAs constant composition layer. We further speculate that since the energy barrier to elastic relaxation by surface deformation has been shown to be much more sensitive to misfit strain ε than the energy barrier to dislocation introduction,[24] it's possible the residual strain in the InGaAs template is increasing an "effective" misfit which controls the competition between the two relaxation mechanisms. This would result in a shift towards favoring elastic relaxation further. Therefore, maximizing relaxation in the tensile mismatched growth templates may be important for minimizing elastic relaxation and surface deformation in ε_t-Ge layers.

CHAPTER 4

Conclusion

In summary, we have grown thin ε_t-Ge layers on different tensile mismatched InGaAs templates specifically to investigate the plastic relaxation occurring in these layers. Our goal was to advance understanding of the strained epitaxy method for creating ε_t-Ge layers which are highly desired for a variety of optoelectronic device applications. Using PV-TEM, we have shown experimentally for the first time that an orthogonal arrays 60° MDs, which are mostly disassociated, exist at the ε_t-Ge /InGaAs interface for ε_t-Ge layers as thin as 15 nm with less than 1% lattice mismatch to the InGaAs template. These are also the first experimental results showing the relationship between the MD spacing, layer thickness, layer mismatch, and the grown-in TDD in the template, for the ε_t-Ge /InGaAs system. We have demonstrated that the mechanisms of plastic relaxation in the ε_t-Ge layer are acutely sensitive to grown-in threading dislocations in the template material and that reducing TDD is critical for maximizing strain retention. Given that ε_t-Ge layer thicknesses of 150+ nm with greater than 1% tensile strain are desired for optoelectronic devices, our work sheds light on the fact that MDs may be inevitable in such layers grown by the strain epitaxy method, and that work is needed to understand the impact of these dislocations on optoelectronic performance.

REFERENCES

1. Sánchez-Pérez, J. R.; Boztug, C.; Chen, F.; Sudradjat, F. F.; Paskiewicz, D. M.; Jacobson, R.; Lagally, M. G.; Paiella, R., Direct-bandgap light-emitting germanium in tensilely strained nanomembranes. *Proceedings of the National Academy of Sciences* **2011,** *108* (47), 18893-18898.

2. Huo, Y.; Lin, H.; Chen, R.; Makarova, M.; Rong, Y.; Li, M.; Kamins, T. I.; Vuckovic, J.; Harris, J. S., Strong enhancement of direct transition photoluminescence with highly tensile-strained Ge grown by molecular beam epitaxy. *Applied Physics Letters* **2011,** *98* (1), 011111.

3. Van de Walle, C. G., Band lineups and deformation potentials in the model-solid theory. *Physical Review B* **1989,** *39* (3), 1871.

4. Sun, X.; Liu, J.; Kimerling, L. C.; Michel, J., Direct gap photoluminescence of n-type tensile-strained Ge-on-Si. *Applied Physics Letters* **2009,** *95* (1), 011911-011911-3.

5. Liu, J.; Sun, X.; Pan, D.; Wang, X.; Kimerling, L. C.; Koch, T. L.; Michel, J., Tensile-strained, n-type Ge as a gain medium for monolithic laser integration on Si. *Optics Express* **2007,** *15* (18), 11272-11277.

6. Nam, D.; Sukhdeo, D.; Roy, A.; Balram, K.; Cheng, S.-L.; Huang, K. C.-Y.; Yuan, Z.; Brongersma, M.; Nishi, Y.; Miller, D., Strained germanium thin film membrane on silicon substrate for optoelectronics. *Optics express* **2011,** *19* (27), 25866-25872.

7. Liu, J.; Cannon, D. D.; Wada, K.; Ishikawa, Y.; Jongthammanurak, S.; Danielson, D. T.; Michel, J.; Kimerling, L. C., Tensile strained Ge pin photodetectors on Si platform for C and L band telecommunications. *Applied Physics Letters* **2005,** *87* (1), 011110-011110-3.

8. Fang, Y.-Y.; Tolle, J.; Roucka, R.; Chizmeshya, A.; Kouvetakis, J.; DCosta, V.; Menendez, J., Perfectly tetragonal, tensile-strained Ge on Ge 1-y Sn y buffered Si (100). *Applied physics letters* **2007,** *90* (6), 061915-061915-3.

9. Currie, M.; Samavedam, S.; Langdo, T.; Leitz, C.; Fitzgerald, E., Controlling threading dislocation densities in Ge on Si using graded SiGe layers and chemical-mechanical polishing. *Applied Physics Letters* **1998,** *72* (14), 1718-1720.

10. Zimmerman, P.; Nicholas, G.; Jaeger, B. D.; Kaczer, B.; Stesmans, A.; Ragnarsson, L. Å.; Brunco, D.; Leys, F.; Caymax, M.; Winderickx, G. In *High performance Ge pMOS devices using a Si-compatible process flow*, Electron Devices Meeting, 2006. IEDM'06. International, IEEE: **2006**; pp 1-4.

11. Miller, D. A., Rationale and challenges for optical interconnects to electronic chips. *Proceedings of the IEEE* **2000,** *88* (6), 728-749.

12. Koo, K.-H.; Cho, H.; Kapur, P.; Saraswat, K. C., Performance comparisons between carbon nanotubes, optical, and Cu for future high-performance on-chip interconnect applications. *Electron Devices, IEEE Transactions on* **2007,** *54* (12), 3206-3215.

13. Bai, Y.; Lee, K. E.; Cheng, C.; Lee, M. L.; Fitzgerald, E. A., Growth of highly tensile-strained Ge on relaxed In(x)Ga(1-x)As by metalorganic chemical vapor deposition. *Journal of Applied Physics* **2008,** *104* (8), 084518.

14. Soref, R. A.; Friedman, L., Direct-gap Ge/GeSn/Si and GeSn/Ge/Si heterostructures. *Superlattices and microstructures* **1993,** *14* (2), 189.

15. Sun, X.; Liu, J.; Kimerling, L. C.; Michel, J., Room-temperature direct bandgap electroluminesence from Ge-on-Si light-emitting diodes. *Optics letters* **2009,** *34* (8), 1198-1200.

16. Clavel, M.; Goley, P.; Jain, N.; Zhu, Y.; Hudait, M. K., Strain-Engineered Biaxial Tensile Epitaxial Germanium for High-Performance Ge/InGaAs Tunnel Field-Effect Transistors.

17. Jakomin, R.; de Kersauson, M.; El Kurdi, M.; Largeau, L.; Mauguin, O.; Beaudoin, G.; Sauvage, S.; Ossikovski, R.; Ndong, G.; Chaigneau, M.; Sagnes, I.; Boucaud, P., High quality tensile-strained n-doped germanium thin films grown on InGaAs buffer layers by metal-organic chemical vapor deposition. *Applied Physics Letters* **2011,** *98* (9).

18. Wirths, S.; Tiedemann, A.; Ikonic, Z.; Harrison, P.; Holländer, B.; Stoica, T.; Mussler, G.; Myronov, M.; Hartmann, J.; Grützmacher, D., Band engineering and growth of tensile strained Ge/(Si) GeSn heterostructures for tunnel field effect transistors. *Applied Physics Letters* **2013,** *102* (19), 192103.

19. People, R.; Bean, J., Calculation of critical layer thickness versus lattice mismatch for GexSi1− x/Si strained-layer heterostructures. *Applied Physics Letters* **1985,** *47* (3), 322-324.

20. Fitzgerald, E., Dislocations in strained-layer epitaxy: theory, experiment, and applications. *Materials science reports* **1991,** *7* (3), 87-142.

21. Matthews, J.; Blakeslee, A., Defects in epitaxial multilayers: I. Misfit dislocations. *Journal of Crystal Growth* **1974,** *27*, 118-125.

22. Dodson, B. W.; Tsao, J. Y., Relaxation of strained-layer semiconductor structures via plastic flow. *Applied Physics Letters* **1987,** *51* (17), 1325-1327.

23. de Kersauson, M.; Prost, M.; Ghrib, A.; El Kurdi, M.; Sauvage, S.; Beaudoin, G.; Largeau, L.; Mauguin, O.; Jakomin, R.; Sagnes, I., Effect of increasing thickness on tensile-strained germanium grown on InGaAs buffer layers. *Journal of Applied Physics* **2013,** *113* (18), 183508.

24. Tersoff, J.; LeGoues, F., Competing relaxation mechanisms in strained layers. *Physical review letters* **1994,** *72* (22), 3570.

25. Maree, P.; Barbour, J.; Van der Veen, J.; Kavanagh, K.; Bulle-Lieuwma, C.; Viegers, M., Generation of misfit dislocations in semiconductors. *Journal of applied physics* **1987,** *62* (11), 4413-4420.

26. Hudait, M. K.; Clavel, M.; Goley, P.; Jain, N.; Zhu, Y., Heterogeneous Integration of Epitaxial Ge on Si using AlAs/GaAs Buffer Architecture: Suitability for Low-power Fin Field-Effect Transistors. *Scientific reports* **2014,** *4*.

27. Dixon, R.; Goodhew, P., On the origin of misfit dislocations in InGaAs/GaAs strained layers. *Journal of applied physics* **1990,** *68* (7), 3163-3168.

28. Kvam, E.; Hull, R., Surface orientation and stacking fault generation in strained epitaxial growth. *Journal of applied physics* **1993,** *73* (11), 7407-7411.

29. Petruzzello, J.; Leys, M., Effect of the sign of misfit strain on the dislocation structure at interfaces of heteroepitaxial GaAsxP1− x films. *Applied physics letters* **1988,** *53* (24), 2414-2416.

30. Hirashita, N.; Sugiyama, N.; Toyoda, E.; Takagi, S.-i., Relaxation processes in strained Si layers on silicon-germanium-on-insulator substrates. *Applied Physics Letters* **2005,** *86* (22), 221923.

31. Hwang, D.; Bhat, R.; Schwarz, S.; Chen, C. In *Partial Dislocations and Critical Thicknesses for Strained Layer Relaxation*, MRS Proceedings, Cambridge Univ Press: **1992**; p 421.

32. Hull, R.; Bean, J.; Peticolas, L.; Bahnck, D., Growth of GexSi1− x alloys on Si (110) surfaces. *Applied physics letters* **1991,** *59* (8), 964-966.

33. Hull, D.; Bacon, D. J., *Introduction to Dislocations*. 5th ed.; Butterworth-Heinemann: **2011**.

34. Williams, D. B.; Carter, C. B., *Transmission Electron Microscopy*. 2nd ed.; Springer **2009**.

35. Hirsch, P. B.; Howie, A.; Nicholson, R.; Pashley, D.; Whelan, M. J., Electron microscopy of thin crystals. *1965, 549 P. BUTTERWORTH INC., 7300 PEARL STREET, WASHINGTON, D. C. 20014* **1966**.

36. Watson, G. P.; Ast, D. G.; Anderson, T. J.; Pathangey, B.; Hayakawa, Y., The measurement of deep level states caused by misfit dislocations in InGaAs/GaAs grown on patterned GaAs substrates. *Journal of applied physics* **1992,** *71* (7), 3399-3407.

37. Fitzgerald, E.; Ast, D.; Kirchner, P.; Pettit, G.; Woodall, J., Structure and recombination in InGaAs/GaAs heterostructures. *Journal of applied physics* **1988,** *63* (3), 693-703.

APPENDIX A

Supporting Figures

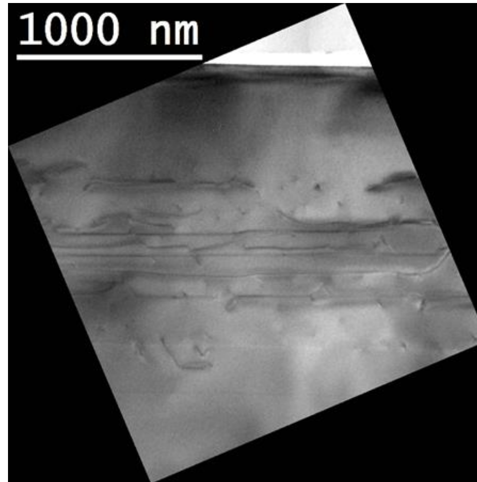

Figure A1. A cross-sectional TEM micrograph of the S2 materials stack showing the depth range of the InGaAs metamorphic buffer which contains a high density of misfit dislocations. The image also shows a smooth 2D surface morphology.

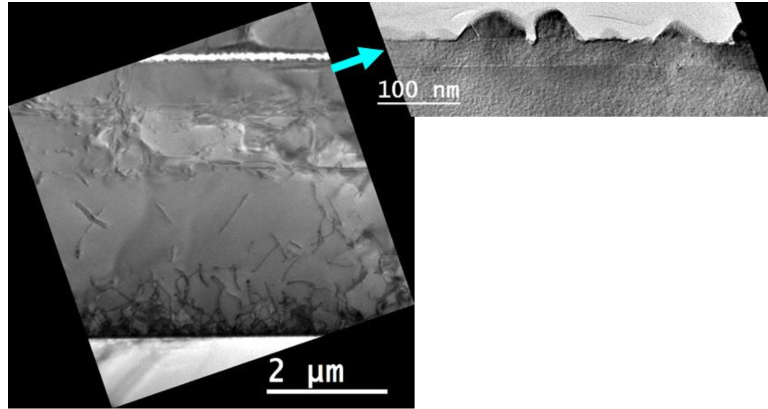

Figure A2. A cross-sectional TEM micrograph of the S3 materials stack. After S3 was grown, a small portion of the S3 wafer was cleaved and returned to the III-V growth chamber. A thin cap of InGaAs was grown to improve carrier confinement for optical characterization. The XTEM foil was prepared from this sample. As shown in the inset image, the InGaAs growth was 3D and the Ge growth was 2D.

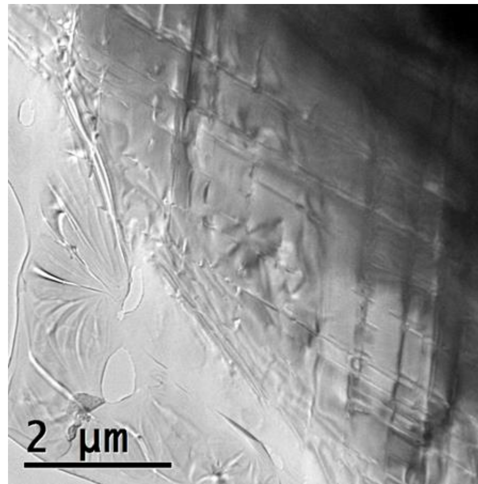

Figure A3. PV-TEM micrograph of a portion of the S2 material stack in which the top 50-100 nm was chemically etched. No bend contours are observed.

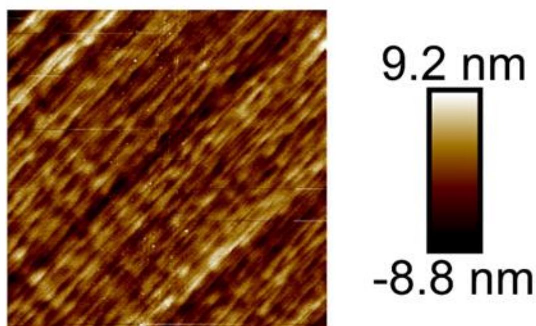

Figure A4. An AFM micrograph showing the surface morphology of the S1 material stack. The image shows a 1D cross-hatch pattern and an array of shallow depressions.

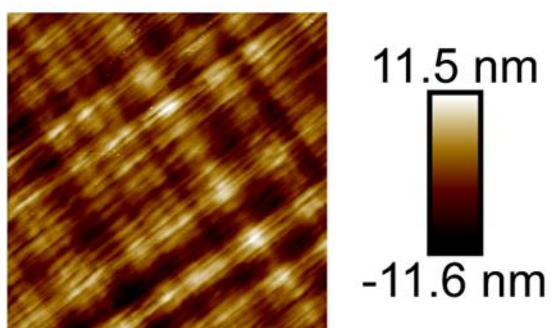

Figure A5. An AFM micrograph showing the surface morphology of the S2 material stack. The image shows a 2D cross-hatch pattern and an array of shallow depressions less pronounced than those shown in Figure A4.